Materials Today Energy 9 (2018) 254–263

Contents lists available at ScienceDirect

Materials Today Energy

journal homepage: www.journals.elsevier.com/materials-today-energy/

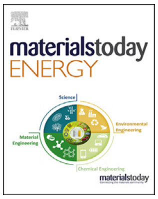

TiO_2 nanofiber photoelectrochemical cells loaded with sub-12 nm AuNPs: Size dependent performance evaluation

Thomas J. Macdonald [a, *], Filip Ambroz [a], Munkhbayar Batmunkh [b, c], Yang Li [a], Dongyoung Kim [d], Claudia Contini [e], Radhika Poduval [d], Huiyun Liu [d], Joseph G. Shapter [b, c], Ioannis Papakonstantinou [d], Ivan P. Parkin [a, **]

[a] Department of Chemistry, University College London, 20 Gordon St, London, WC1H 0AJ, United Kingdom
[b] College of Science and Engineering, Flinders University, Bedford Park, South Australia, 5042, Australia
[c] Australian Institute for Bioengineering and Nanotechnology, University of Queensland, St Lucia, Queensland, 4072, Australia
[d] Department of Electronic and Electrical Engineering, University College London, Torrington Place, London, WC1E 7JE, United Kingdom
[e] Department of Chemistry, Imperial College London, Imperial College Road, London, SW7 2AZ, United Kingdom

ARTICLE INFO

Article history:
Received 26 March 2018
Received in revised form
31 May 2018
Accepted 4 June 2018

Keywords:
Nanofibers
Photoelectrodes
Photoelectrochemical cell
Titanium dioxide
Gold nanoparticles
Plasmonics

ABSTRACT

Incorporation of gold nanoparticles (AuNPs) into titanium dioxide (TiO_2) photoelectrodes has been used traditionally to increase the performance of photoelectrochemical cells (PECs) through their tailored optical properties. In contrast to larger AuNPs, previous studies have suggested that smaller AuNPs are the most catalytic or effective at increasing the photovoltaic (PV) performance of TiO_2 photoelectrodes based on PECs. Despite this, AuNPs are often only compared between sizes of 12–300 nm in diameter due to the most common synthesis, the Turkevich method, being best controlled in this region. However, the optimum radius for citrate-capped AuNPs sized between 5 and 12 nm, and their influence on the PV performances has not yet been investigated. In addition to using AuNPs in the photoelectrodes, replacing traditional TiO_2 NPs with one-dimensional nanofibers (NFs) is a promising strategy to enhance the PV efficiency of the PECs due their capability to provide a direct pathway for charge transport. Herein, we exploit the advantages of two different nanostructured materials, TiO_2 NFs and sub-12 nm AuNPs (5, 8, 10, and 12 nm), and fabricate composite based photoelectrodes to conduct a size dependent performance evaluation. The PECs assembled with 8 nm AuNPs showed ~20% improvement in the average power conversion efficiency compared to the control PECs without AuNPs. The highest performing PEC achieved a power conversion efficiency of 8%, which to the best of our knowledge, is among the highest reported for scattering layers based on pure anatase TiO_2 NFs. On the basis of our comprehensive investigations, we attribute this enhanced device performance using 8 nm AuNPs in the TiO_2 NF photoelectrodes to the improved spectral absorption, decreased series resistance, and an increase in electron transport and injection rate leading to an increase in current density and fill factor.

1. Introduction

Titanium dioxide (TiO_2) is the most extensively studied metal oxide semiconductor and is well-known for its chemical stability, environmental compatibility and low production cost [1,2]. With electrons as its majority carriers, the importance of TiO_2 in photocatalysis relies on its ability to oxidize oxygen or organic materials [3,4]. The high photocatalytic activity of TiO_2 is based upon the reduction and oxidation potentials situated within its wide band-gap. This allows for its use in a wide range of applications including artificial photosynthesis [5] and photoelectrochemical cells (PECs) [6]. For TiO_2 and its application in PECs, one of the most important discoveries is the dye-sensitized solar cells (DSSC); one of the promising third generation solar cells [2,7,8]. DSSCs are a PEC which typically consist of a TiO_2 photoelectrode, and a platinum counter electrode, separated by a liquid electrolyte containing either iodide/triiodide I^-/I_3^- or cobalt(II/III)-based redox mediators [2,9]. While several groups have now

---

* Corresponding author.
** Corresponding author.
E-mail addresses: tom.macdonald@ucl.ac.uk (T.J. Macdonald), i.p.parkin@ucl.ac.uk (I.P. Parkin).

https://doi.org/10.1016/j.mtener.2018.06.005

replaced the liquid electrolyte with solid state hole transport materials such as Spiro-MeOTAD [10], solid-state DSSCs are typically less efficient than liquid electrolyte-based DSSCs with the highest performance to date being 11% [8]. Although state-of-the-art liquid electrolyte-based DSSCs have achieved remarkable efficiencies of 13% for porphyrin-sensitized [11], and 14% for silyl-anchor and carboxy-anchor dyes [12], TiO_2 nanoparticulate-based PECs suffer from the following drawbacks: (i) limited charge transport [13], (ii) poor absorption of low energy photons [14], and (iii) high charge recombination [15]. The limited charge transport of nanoparticulate TiO_2 PECs can be reduced by substituting nanoparticles (NPs) for one-dimensional (1D) nanofibers (NFs), which have been previously shown to reduce the scattering of free electrons by reducing the grain boundaries of the interconnected TiO_2 NPs [13]. Our previous work has shown that the incorporation of TiO_2 NFs (and other 1D inorganic nanostructures) in both DSSCs and solid-state perovskite solar cells enables fast electron transport by offering enhanced directionality from the 1D structures [16,17].

On the other hand, spherical noble metal nanostructures such as gold nanoparticles (AuNPs) show several beneficial effects related to light trapping (scattering), fluorescence and local field enhancement, facilitating charge separation and charge transfer, all of which are extremely important in DSSC devices [18–21]. Not surprisingly, all these effects are related to the tailored optical properties and previous studies have suggested three methods of light trapping which result in enhanced DSSC performance using noble metal NPs; 1) trapping incident light inside thin films *via* scattering elements, 2) energy localization in the near field of the NP, and 3) charge-propagation kinetics at the noble metal NP/TiO_2 interface from the surface plasmon polariton waves [19]. The plasmonic properties in AuNPs are tunable which enables controlled manipulation of the optical properties over the visible spectral range in a variety of photovoltaic devices. AuNPs have previously been incorporated into both the active and scattering layer of TiO_2 in DSSCs [18,22,23]. Regardless of the layer in which AuNPs are incorporated, the observed increase in performance is mainly from an enhanced photocurrent density of the DSSCs containing AuNPs [19]. This performance improvement has been previously related to increased dye-loading due to superior surface area coverage [24], but is more commonly attributed to the plasmonic effect of the AuNPs [19]. Literature has also shown that the amount of AuNPs added to a DSSC system is very important and an excess will result in a decrease in performance or interact with the electrolyte causing problems such as recombination of charge carriers. Heavy loadings (>1.0 wt%) of metal NPs (Ag and Au) have previously been shown to increase the probability of aggregation between the metal NPs in the composite films [21]. In addition to the use of metal NPs, TiO_2 only absorbs in the UV-region and as a result, a light absorbing material (such as a molecular dye) is usually introduced. The most common dye used in DSSCs is the ruthenium-based dye molecule (known as N719) and given its strong absorption band at 530 nm aligns well with the surface plasmonic resonance of AuNPs sized between 5 and 50 nm in diameter (515–540 nm). Notably, red shifting the absorption too far causes dimerization and would no longer contribute to an increase in efficiency. Other than loading amounts, size effects also play a crucial role in performance enhancement. Wang et al. investigated DSSCs loaded with 5, 45, and 110 nm AuNPs and compared their performance [19]. They showed that 40 nm AuNPs show the highest photocurrent due to the perfectly matched absorbance overlap with N719. However, DSSCs loaded with the smallest AuNPs (5 nm in diameter) has the highest power conversion efficiency (PCE). Typically, smaller AuNPs have reduced light scattering effects (scattering cross section) but higher light absorption (absorption cross section). On the other hand, a collection of small AuNPs will scatter more than a single large AuNP. These plasmonic features of small AuNPs (or a collection of AuNPs) can contribute to improved electron collection originating from the increased electron lifetimes and this contributes considerably to the overall performance enhancement [19].

While the combination of plasmonic NPs with TiO_2 to enhance the performance of PECs is well established, small AuNPs are commonly seen as the most catalytic in PECs (for reasons described earlier) [25]. While other synthetic approaches have successfully developed protocols to make sub-12 nm AuNPs, they typically use insulating capping ligands such as polyvinylpyrrolidone (PVP) [25], poly(ethylene glycol) (PEG) [26], polymeric stabilizes [27], strong surfactants [28], and other thiol stabilized moieties [29]. Long chained ligands and hydrophobic thiol coatings have limited capability with TiO_2 PECs, since they will either be insulating or insoluble. An approach by Piella et al. [30] encompasses a kinetically controlled seeded growth strategy to enable the production of sub-12 nm citrate stabilized AuNPs in water, making them fully compatible with TiO_2 photoelectrodes.

Herein, we utilize the advantages of two different nanostructured materials, TiO_2 NFs and AuNPs, and fabricate composite based photoelectrodes on fluorine doped tin oxide (FTO), in which TiO_2 NFs act as strong light scattering layer loaded with size controlled sub-12 nm AuNPs. A schematic of the composite PEC is illustrated in Scheme 1, where a scanning electron microscopy (SEM) image of the TiO_2 NF layer is rendered to visualize the lawn-like architecture. This work is the first example where the PEC performance of TiO_2 NF photoelectrodes has been finely tuned using sub-12 nm AuNPs to determine the smaller size limits for enhancing the performance of NF-based PECs. We describe a simple route to fabricate electrospun electrodes for PECs and explore how the addition of size controlled sub-12 nm AuNPs into the electrospun scattering layer can improve the performance in a PEC system.

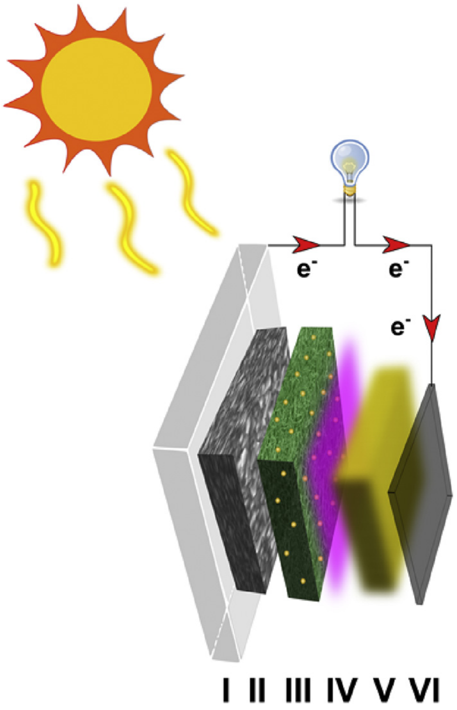

Scheme 1. Schematic represents the TiO_2 NF photoelectrode loaded with AuNPs and its assembly into a PEC. The assembly is represented by I: FTO, II TiO_2 NPs (active layer), III AuNP-TiO_2 NFs (scattering layer), IV: ruthenium dye molecules (N719), V: iodide-based electrolyte, and VI: FTO/platinum.

2. Experimental section

2.1. Materials

All chemicals were purchased from Sigma Aldrich (United Kingdom) unless otherwise noted. The sizes of the nanoparticles quoted always refer to the diameter of the particles.

2.2. Synthesis of AuNPs

5 nm AuNPs were synthesized following a procedure previously reported by Piella et al. [30] In a typical synthesis, a 150 mL aqueous solution of sodium citrate (SC, 2.2 mM) containing 0.1 mL of tannic acid (2.5 mM) and 1 mL of potassium carbonate (K_2CO_3, 150 mM) was heated to 70 °C with vigorous stirring. Upon reaching 70 °C, 1 mL of tetrachloroauric acid ($HAuCl_4$, 25 mM) was quickly injected which resulted in an immediate color change from clear to black, and then to soft pink. The solution was kept at the same temperature for 10 min to ensure complete reduction of the gold precursor. A small aliquot of the solution was removed from the reaction vessel and used for UV–Vis, TEM, and for the incorporation into TiO_2 photoelectrodes.

2.3. Growth of AuNPs

AuNPs of 8, 10, and 12 nm were then subsequently grown from the 5 nm AuNP solution (described in the previous section). The 5 nm AuNP solution was diluted by extracting 55 mL and adding another 55 mL of SC (2.2 mM). The solution was then heated again to 70 °C, and two injections of 0.5 mL $HAuCl_4$ (25 mM) were added (in 10-minute intervals). This growing step was repeated until the desired particle sizes were reached. The particles had a concentration of 7×10^{13} NP mL^{-1} and were stored in a dark cool place.

2.4. Preparation of TiO_2 NFs

TiO_2 NFs were prepared according to our previous reports [16,17]. Briefly, TiO_2 NFs were electrospun from a sol–gel solution containing titanium(IV) butoxide (TBO, 0.5 g), poly(vinyl pyrrolidone) (PVP, 1 g), and absolute ethanol (10 mL). The TiO_2 sol–gel was electrospun at a voltage of 10 kV with a flow rate of 1 mL per hour and the collection plate was maintained at a distance of 20 cm. Once enough fiber mats had been obtained, the PVP coated TiO_2 NFs were subject to pyrolysis at 500 °C to remove PVP.

2.5. Preparation of TiO_2 NF photoelectrodes

For control samples, pure TiO_2 NFs (0.5 g) were mixed with ethanol (20 mL) and the mixture was sonicated for at least 2 h, until no fiber agglomerates could be seen. Once a uniform white solution was achieved, 2 mL of terpineol was added and the mixture was sonicated for a further 15 min. Finally, ethanol was removed by rotary evaporation to yield a white paste of TiO_2 NFs. The TiO_2 NF paste was then stored until it was required. Transparent TiO_2 photoanodes were prepared by doctor blading TiO_2 nanoparticle paste (GreatCell Solar, DSL-18NRT) onto fluorine-doped tin oxide (FTO). The transparent photoelectrodes were sintered at 500 °C to remove all organic binders from the paste and form a uniform transparent TiO_2 NP anatase active layer. The photoelectrodes were then subject to treatment in titania tetrachloride ($TiCl_4$, 40 mM) for 45 min at 70 °C. The photoelectrodes were then thoroughly washed with Milli-Q water and sintered at 500 °C. A thinner opaque scattering layer of TiO_2 NFs was then added on top of the transparent layer, using the same technique. The photoelectrodes were again sintered at 500 °C to remove all organic binders from the NF paste. Notably, the $TiCl_4$ treatment was only used on the transparent layer, not the scattering layer. For samples that incorporated AuNPs, 0.5 wt% of each NP size variation was added to the TiO_2 NF pastes (scattering layer only) and the same fabrication procedure was followed. Note, 0.5 wt% was calculated on the pure mass of TiO_2 NFs and not the paste mass. The loading of 0.5 wt% was chosen as previous work has demonstrated loadings of 0.5 wt% to be the most effective in similar systems, where exceeding 1 wt% loading of AuNPs has been shown to decrease the performance of PECs [21]. The loading of 0.5 wt% AuNPs was kept constant for all photoelectrodes used in this work.

2.6. Photoelectrochemical cell fabrication

Directly after sintering, the warm photoelectrodes (TiO_2 NP/AuNP-TiO_2 NFs) with a total cell area of 0.125 cm^2 were sensitized with an absolute ethanol solution of ruthenizer 535-bisTBA (Solaronix, 0.5 mM) for 20 h in the dark. The sensitized photoelectrodes were dark purple in color and were then carefully washed with ethanol to remove any unanchored dye molecules from the surface. Sensitized photoelectrodes were eclipsed onto platinum-coated FTO (GreatCell Solar) and sealed with Low Temperature Thermoplastic Sealant (GreatCell Solar, MS004610). The electrodes were heated to 100 °C for 15 min to seal the sealant. The iodide-based redox mediator (iodine (I_2, 0.05 M), Lithium Iodide (LiI, 0.1 M), 1,2-dimethyl-3-propylimidazolium iodide (DMPII, 0.6 M), and 4-tert-Butylpyridine (TBP, 0.5 M) in acetonitrile) was injected into the freshly sealed electrodes by vacuum filling.

2.7. Materials chemistry and characterization

All details for the materials chemistry and photovoltaic characterization can be found in the Supporting information.

3. Results and discussion

Each batch of AuNPs was characterized using UV–visible (UV–Vis) absorbance spectroscopy and transmission electron microscopy (TEM) (Fig. 1). A UV–Vis absorbance spectrum of each of the different sized AuNPs is shown in Fig. 1a. The localized surface plasmon resonance (LSPR) peak for 5, 8, 10 and 12 nm were 512, 515, 517, and 519 nm respectively, where the red shift in absorbance is consistent with an increase in particle size [30]. All LSPR peaks had similar full-width half maximums (FWHM), and the AuNP concentration was ~7×10^{13} NPs mL^{-1}. Furthermore, the absorbance edge of the LSPR peak, slightly overlaps with the peaks for our light absorbing dye-molecule N719 (in ethanol), which can be seen in Fig. 1a. This suggests that any improvement in light harvesting can be partially due to the plasmonic effect of the AuNPs. The size distribution of the AuNPs was calculated by generating a series of histograms from measuring the size of many AuNPs over several areas on the TEM grid (Fig. 1b). The particle size distribution for 5, 8, 10 and 12 nm was 0.6 (FWHM: 1.3), 0.7 (FWHM: 1.6), 0.8 (FWHM: 1.9), and 1.0 (FWHM: 2.5) nm respectively, where the standard deviation of the AuNP size increases with the size of the nanoparticles [30], which is a typical incremental pattern for seed-initiated growth of AuNPs. The TEM images used for the particle counting are shown in Figs. S1–S4 in the Supporting information. The corresponding TEM, depicted in Fig. 1c, shows that all AuNPs are spherical in shape and highly crystalline with lattice separation of 0.21 and 0.23 nm, indicative of the {200} and {111} planes respectively [31]. The AuNPs were stored in a cool dark place and remained freely dispersed in water for several months without showing any signs of aggregation.

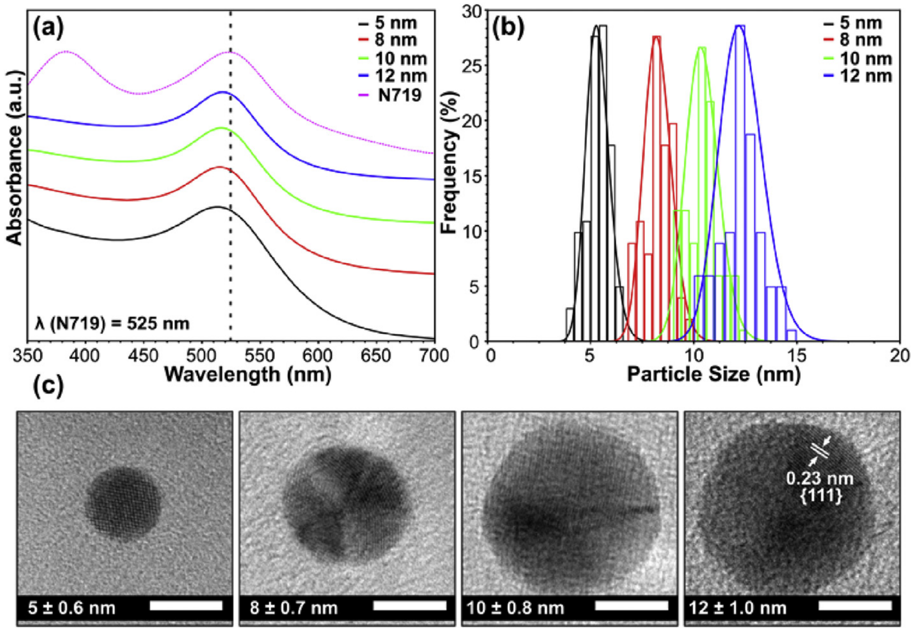

Fig. 1. (a) UV–visible absorption spectra of 5, 8, 10, and 12 nm AuNPs and N719 dye solution. (b) Histograms for the particle size distributions measured from TEM images by counting over multiple grid areas consisting of at least 100 NPs. (c) The correlating TEM images of the AuNPs, confirming high crystallinity. The scale bar on the TEM images is 5 nm.

TiO_2 NFs were synthesized and worked into a screen printable paste *via* our previous method [16]. Additional TiO_2 NF pastes were prepared and individually doped with 5, 8, 10, and 12 nm citrate stabilized AuNPs. This NF-based paste was then used as a scattering layer in our photoelectrode. All photoelectrodes were assembled on FTO with an underlying active layer of TiO_2 NPs. One dimensional (1D) nanostructures often suffer from poor dye loading, where in NFs, dye uptake decreases as a function of fiber diameter [32]. Therefore, the active layer was prepared using TiO_2 NPs to ensure the sufficient attachment of N719 dye molecules for our PECs. A schematic of the complete PEC assembly can be seen in Scheme 1. The cross-sectional scanning electron microscopy (SEM) image of the TiO_2 NP/AuNP-TiO_2 NF photoelectrodes is shown in Fig. 2a. The total thickness of the electrodes was 13 μm, verified using a step-profile meter. The cross-section is made up of three main parts, 'I' represents the FTO, 'II' shows the 8 μm active layer of TiO_2 NPs, and 'III' illustrates the 5 μm scattering layer of AuNP-TiO_2 NF photoelectrodes. These thicknesses align with the highest performing PECs, where the thicker active layer provides effective dye adsorption [33], and the thinner scattering layer enables efficient light scattering. To image the AuNPs in the TiO_2 NF layer, high-resolution (HR) SEM of the TiO_2 NP/AuNP-TiO_2 NF photoelectrodes is shown in Fig. 2b. The TiO_2 NFs had diameters between 200 and 500 nm and were several microns in length. Despite the use of HR-SEM, the AuNPs were not visible in Fig. 2b, which we attribute to the low concentration of AuNPs added (0.5 wt%) [19]. In order to visualize the AuNPs in the TiO_2 NFs, HR-TEM was used to characterize the composite material (Fig. 2c). While the contrast makes it difficult to pin-point a single AuNP within the NFs, elemental mapping confirmed the presence of the AuNPs within the TiO_2 NFs (see Fig. 2c).

To further verify the presence of the AuNPs in the TiO_2 NF layer of the photoelectrodes, X-ray Photoelectron Spectroscopy (XPS) was performed and the results are shown in Fig. 3a and b. To ensure AuNPs were not only attached to the surface, a monatomic depth profile of the TiO_2 NP/AuNP-TiO_2 NF photoelectrodes was measured. Depth profiling involved using a calibrated ion beam to etch layers of the photoelectrode, revealing subsurface information. The etching was performed for 400 s which corresponded to a penetration of ~100 nm into the surface of the electrode. The depth profile analysis was performed to review sub-surface information and confirm the presence of the AuNPs embedded inside the TiO_2 NFs. Fig. 3a verified the TiO_2 by the Ti2p peaks present at binding energies 464 eV and 458 eV, indicative of $Ti2p_{(1/2)}$ and $Ti2p_{(3/2)}$, respectively. The presence of AuNPs was verified in Fig. 3b at binding energies of 83.7 eV, and 87.5 eV, indicative of $Au4f_{(7/2)}$ and $Au4f_{(5/2)}$, respectively. AuNP peaks in 4f regions correspond to a spin orbital splitting of 3.8 eV. Previous studies of AuNPs on TiO_2 show that for $Au^{+}4f_{(7/2)}$ and $Au^{3+}4f_{(7/2)}$, there is a significant shift towards higher binding energies 84.4 eV and 86.5 eV [34,35]. Fig. 3b clearly shows only one species for the $Au4f_{(7/2)}$ 83.7 eV that is most closely matched with metallic Au^{0} which is typically present at 84.0 eV. The negative shift of 0.3 eV for $Au^{0}4f_{(7/2)}$ has been attributed to strong interactions between the Au in the TiO_2 framework [35]. Measuring the XPS of AuNPs at such low concentrations is challenging and we attribute their low concentration (0.5 wt%) to be the reason for the noisy Au4f spectrum, which has been reported before [36]. Surface scans for the Au4f peaks, confirming the presence of AuNP at the surface, can be seen in the Supporting information, Fig. S5. The surface scan measurements confirm the presence of AuNPs on the surface and the depth profile measurements confirm that the AuNPs are also within the porous TiO_2 NF matrix. The anatase phase of the TiO_2 was maintained throughout doping. This was investigated using X-ray diffraction (XRD) where the JCPDS card number was confirmed for anatase TiO_2 (JCPDS card number 21-1272). The peaks not assigned to the anatase phase of TiO_2 can be assigned to the FTO (Fig. 3c). While no shifting in the diffraction pattern was seen, the TiO_2 NP/AuNP-TiO_2 NF photoelectrodes showed slight broadening of the XRD peaks which can be attributed to the incorporation of AuNPs into the TiO_2 lattice [13]. Furthermore, mesoporous TiO_2 structures which have low AuNP content (<0.5%) have previously been shown not to exhibit any Au characteristic diffraction, whereby changes are typically observed with increasing Au content and/or increasing particle size [35]. Since the XRD pattern is typically only associated with long range order of structural arrangements, UV–Vis measurements

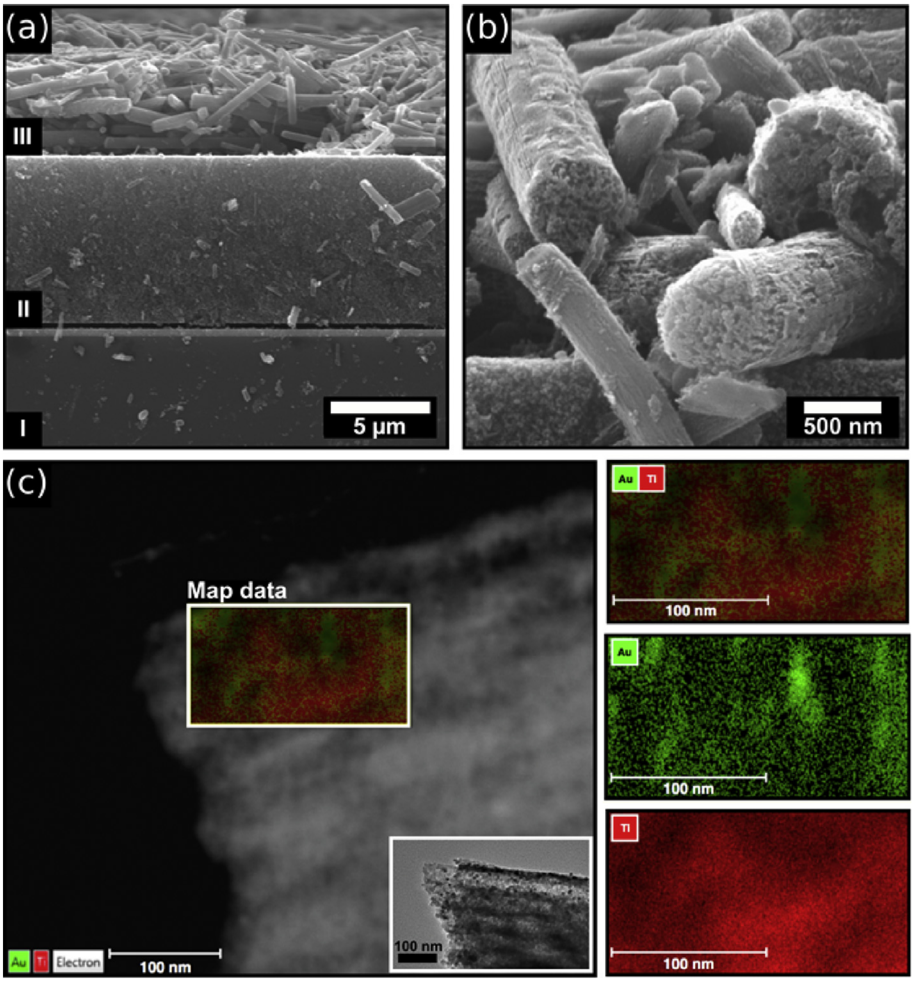

Fig. 2. (a) Cross sectional SEM image of FTO/TiO_2 NP/AuNP-TiO_2 NF photoelectrodes. Where I: FTO, II: TiO_2 NPs, and III: AuNP-TiO_2 NFs. (b) SEM image of AuNP-TiO_2 NF scattering layer, (c) TEM image of AuNP-TiO_2 NFs with elemental mapping inset. RHS images show the corresponding mapped elements with Au and TiO_2 represented in green and red respectively. (For interpretation of the references to color in this figure legend, the reader is referred to the Web version of this article.)

confirmed that the absorbance edge for both TiO_2 and TiO_2/AuNP NF electrodes did not change, Fig. 3d. No SPR peak was visible in the TiO_2 NP/AuNP-TiO_2 NF photoelectrodes, and this was again attributed to the low concentration of AuNPs present in the NFs. The inset of the UV–Vis measurements shows the Tauc plot, confirming the band gap of the electrode is 3.15 eV for both TiO_2 NF control and AuNP-TiO_2 NF, which are expected to exhibit similar open-circuit voltage (V_{oc}) values in the PECs. To gain further insight to the optical features of our TiO_2 NP/AuNP-TiO_2 NF photoelectrodes, Raman spectroscopy was also performed. The Raman spectra of both pure TiO_2 and TiO_2 NP/AuNP-TiO_2 NF photoelectrodes are shown in Fig. S6 (SI). Both TiO_2 and TiO_2 NP/AuNP-TiO_2 NF photoelectrodes show the TiO_2 Raman active vibration modes E_g (143 cm^{-1}), A_{1g} (395 cm^{-1}), B_1 (514 cm^{-1}), and an overtone at E_g (639 cm^{-1}). Vibrational mode E_g (143 cm^{-1}), distinctly identifies the anatase phase for both TiO_2 NP/TiO_2 NF control and TiO_2 NP/AuNP-TiO_2 NF photoelectrodes where the decrease in intensity and slight peak broadening for the AuNP containing photoelectrode can be attributed to surface adsorbed AuNPs [23]. This was confirmed over several points on the photoelectrode, where the height of the sample was kept constant for both TiO_2 NP/TiO_2 NF control and TiO_2 NP/AuNP-TiO_2 NF photoelectrodes. The results for the Raman measurements suggest a slight increase in crystalline defects where the AuNPs incorporated into the TiO_2 NFs provide additional photoelectron trapping centers which helps to reduce charge recombination, a major problem in TiO_2 based PECs [35].

The photovoltaic performance of TiO_2 NP/TiO_2 NF control and TiO_2 NP/AuNP-TiO_2 NF photoelectrodes (containing 5, 8, 10, and 12 nm AuNPs) were analyzed under 1 sun conditions (AM 1.5 simulated sunlight). The ***J*–*V*** characteristics and incident photon to current conversion efficiency (IPCE) are plotted in Fig. 4 and the corresponding photovoltaic properties of each device have been tabulated in Table 1. The TiO_2 NF control devices achieved a short-circuit current density ($\boldsymbol{J}_{SC}$) of 15.8 mA cm^{-2}, an open-circuit voltage ($\boldsymbol{V}_{OC}$) of 757.9 mV, fill factor (FF) of 57.7% and overall power conversion efficiency (PCE) of 6.7%. Interestingly the highest performing device was that containing 8 nm AuNPs, where the best device achieved a $\boldsymbol{J}_{SC}$ of 17.4 mA cm^{-2}, $\boldsymbol{V}_{OC}$ of 745.7 mV, FF of 62.4% and PCE of 8.0%. The 19.4% improvement in PCE for the TiO_2 NP/AuNP-TiO_2 NF (8 nm) device can be attributed to the increase in $\boldsymbol{J}_{SC}$ and FF, consistent with previous reports [20,37]. The $\boldsymbol{J}_{SC}$ and FF for the TiO_2/AuNP-TiO_2 NF (8 nm) device improved by 10% and 8%, respectively when compared to the control device. The addition of 5 nm AuNPs in the TiO_2 NP/AuNP-TiO_2 NF photoelectrodes also resulted in an enhancement in $\boldsymbol{J}_{SC}$ (16.6 mA cm^{-2}) and FF. Surprisingly, additions of 10 and 12 nm AuNPs decreased the $\boldsymbol{J}_{SC}$ (Fig. 4a) but still increased the FF. The increase in the $\boldsymbol{J}_{SC}$ for the 5 and 8 nm TiO_2 NP/AuNP-TiO_2 NF photoelectrodes can be attributed

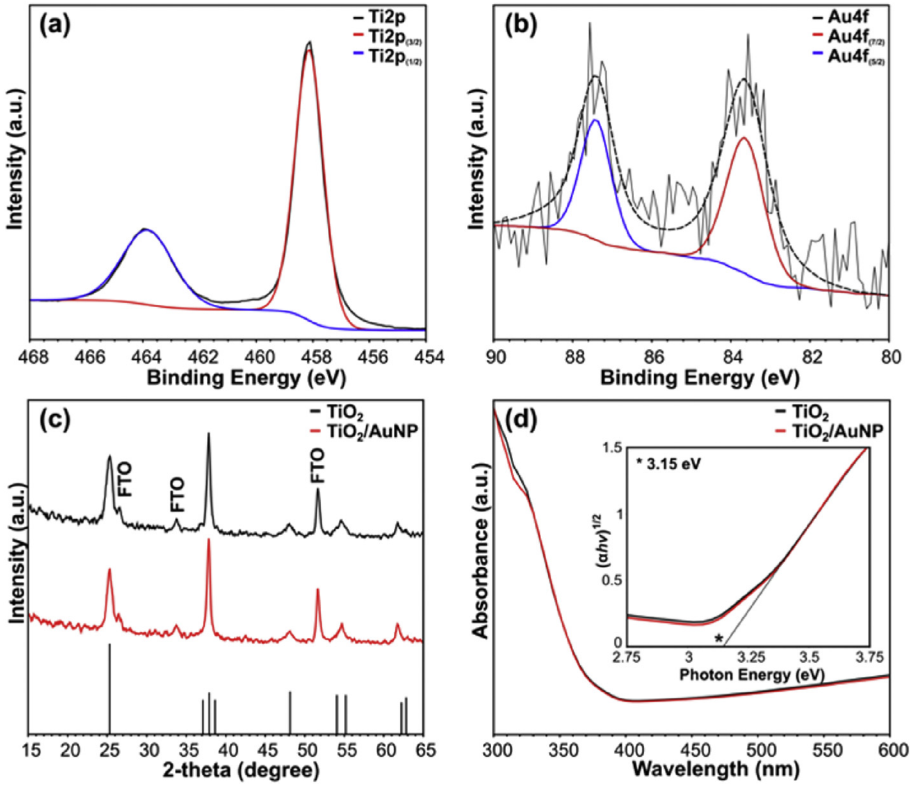

Fig. 3. X-ray photoelectron spectroscopy (XPS) for Ti2p (a) and Au4f (b). All peaks were fitted using CasaXPS software. (c) shows the X-ray diffraction (XRD) spectra for TiO_2 and TiO_2/AuNP NF PECs confirming the anatase crystal structure (JCPDS card number 21-1272). (d) shows the UV–visible (UV–vis) absorption spectroscopy where the inset shows the Tauc plot confirming the band gap for TiO_2.

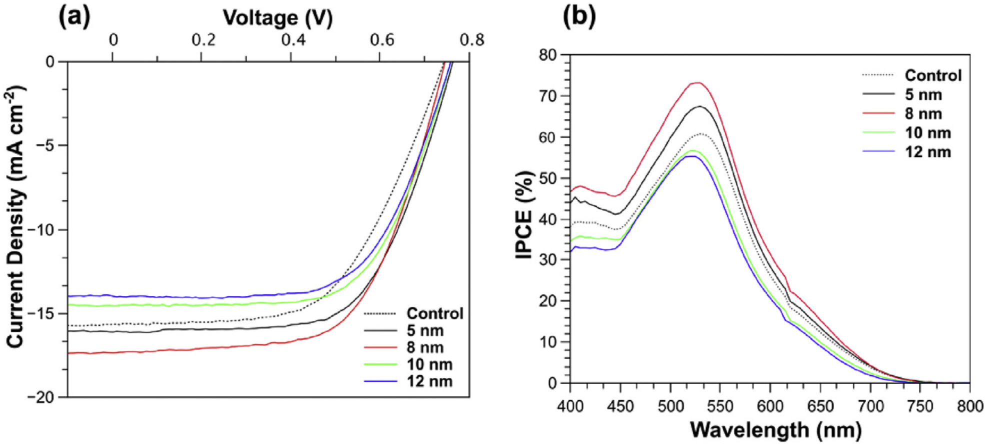

Fig. 4. (a) ***J*–*V*** characteristics of TiO_2 NP/TiO_2 NF AuNP containing (5, 8, 10, 12 nm) PECs. The ***J*–*V*** curves were collected by sweeping in the reverse direction between 1.0 V and −0.2 V. (b) the IPCE spectra of the devices where the spectra were calibrated by a silicon reference cell and collected between the region of 400–800 nm. (For interpretation of the references to color in this figure legend, the reader is referred to the Web version of this article.)

Table 1
Summary of photovoltaic parameters for the highest performing devices. The table represents 5 different PECs including control, 5, 8, 10, and 12 nm AuNP NF PECs.

PEC	J_{SC} (mA cm^{-2})	V_{OC} (mV)	FF (%)	PCE (%)
Control TiO_2 NFs	15.8	757.9	57.7	6.7
5 nm AuNPs	16.6	763.4	63.0	7.7
8 nm AuNPs	17.4	745.7	62.4	8.0
10 nm AuNPs	14.8	758.9	63.9	7.1
12 nm AuNPs	14.0	761.7	65.6	6.8

to the more favorable surface area of the sub-12 nm plasmonic NPs [25]. Wang et al. [19] previously showed that photocharging, light scattering, and the LSPR effect all co-exist as factors causing the increase in performance of TiO_2 NP/AuNP-TiO_2 NF photoelectrodes, but are selectively dominant in different sizes of AuNPs, whereby they report 5 nm AuNPs to be the highest performing when compared to 45 and 110 nm AuNPs [19]. While previous results in similar systems have suggested that the $\boldsymbol{V}_{OC}$ increases with decreasing particle size, our results show the $\boldsymbol{V}_{OC}$ stays relatively constant for all devices. We attribute our result to the amount of AuNPs added being too low to have any upward shift on the Fermi level [19], and given our small size increments, any change in $\boldsymbol{V}_{\mathrm{OC}}$ would be difficult to observe. This is in good agreement with what we have seen from our Tauc plot (Fig. 3d). Furthermore, adding low amounts of AuNPs has been shown to be far more beneficial than larger loadings due to the genuine concern of electrolyte attack on metal AuNPs [20,38].

The FF substantially increased for all devices containing the AuNPs. This increase in the FF value is commonplace for TiO_2 NP/AuNP-TiO_2 NF photoelectrodes and has been frequently attributed to a reduction in the charge recombination [19,20]. Electron effective lifetime and the recombination resistance have been previously shown to decrease as AuNP size increases and there is a suppression of interfacial recombination compared with the control photoelectrodes [19]. Therefore when AuNPs are present, previous studies show longer electron lifetimes which correlates to the longer existence of free electrons in the conduction band of the TiO_2, thus reducing the chances of recombination in the PEC [19]. Unsurprisingly, the overall PCE was higher for all devices containing AuNPs mainly due to the higher FF value as compared to the control cells. To further investigate the enhancement in $\boldsymbol{J}_{\mathrm{SC}}$, the IPCE for the PECs was measured (Fig. 4b). The addition of 8 nm AuNP resulted in a peak IPCE value of 73%, compared to 60% for the control PECs. This 13% improvement in peak IPCE value shows that when 8 nm AuNPs are incorporated into a TiO_2 NF scattering layer, there is a significant optoelectronic benefit, and this is reflected in the overall enhancement in the efficiency. Furthermore, there is a slight red shift in the peak maximum for the IPCE curve in the TiO_2 NP/AuNP NF PEC. The slight red shift in the IPCE is due to the enhanced light absorption of dye molecules and AuNPs assist in absorption towards the red portion of the solar spectrum. This has also been verified in previous studies where the presence of AuNPs in the scattering layer have been found to enhance the solar radiation absorption in the higher wavelength range [39].

The average photovoltaic parameters ($\boldsymbol{J}_{\mathrm{SC}}$, $\boldsymbol{V}_{\mathrm{OC}}$, FF, and PCE) and their standard error are depicted in Fig. 5. The average photovoltaic parameters follow the same trend as all the highest performing devices summarized in Table 1, which confirms the high reproducibility of the PECs. The photovoltaic parameters were plotted between the corresponding minimum and maximum values in order to get a better representation of improvement (Fig. 5). For the highest performing TiO_2 NP/AuNP-TiO_2 NF photoelectrodes containing the 8 nm AuNPs, the biggest improvement can be seen from the increase in $\boldsymbol{J}_{\mathrm{SC}}$ and FF. Interestingly, the $\boldsymbol{V}_{\mathrm{OC}}$ stayed relatively consistent with the somewhat larger standard error being attributed to the volatile and temperature sensitive liquid-based electrolyte. Due to the significant increase in $\boldsymbol{J}_{\mathrm{SC}}$ and FF, the average PCE for the control devices was improved by 20% upon addition of 0.5 wt% 8 nm AuNPs. To gain further understanding into the performance enhancement, the average resistance measurements for all devices were compiled into Table S1 in the SI. The series resistance (R_S) for the 5, 8, and 10 nm containing TiO_2 NP/AuNP NF devices was lower than that for the control devices. The lowest R_S was found in the TiO_2 NP/AuNP NF device containing the 8 nm AuNPs, which supports it being the highest performing. Typically, lowering the R_S results in an increase in FF and while this is consistent for the TiO_2 NP/AuNP NFs devices containing the 5, 8, and 10 nm AuNPs, the 12 nm AuNP devices show a considerable increase in R_S. Interestingly, the $\boldsymbol{J}_{\mathrm{SC}}$ for this device was lower than all other devices and this can therefore be attributed to the significant increase in R_S. It is well known that small AuNPs can have catalytic properties and the lowering of the R_S may indicate that the small particles are effective at catalyzing the oxidation of the I^- at the photoanode to regenerate the dye molecule. The catalytic effects for AuNPs are very size dependent so we postulate that the catalytic effect of the 12 nm particles is much reduced. No trends were found in the shunt resistance (R_{SH}) where the R_{SH} remained within an order of magnitude of each other for all devices. Significant power losses due to low R_{SH} values are attributed to fabrication defects

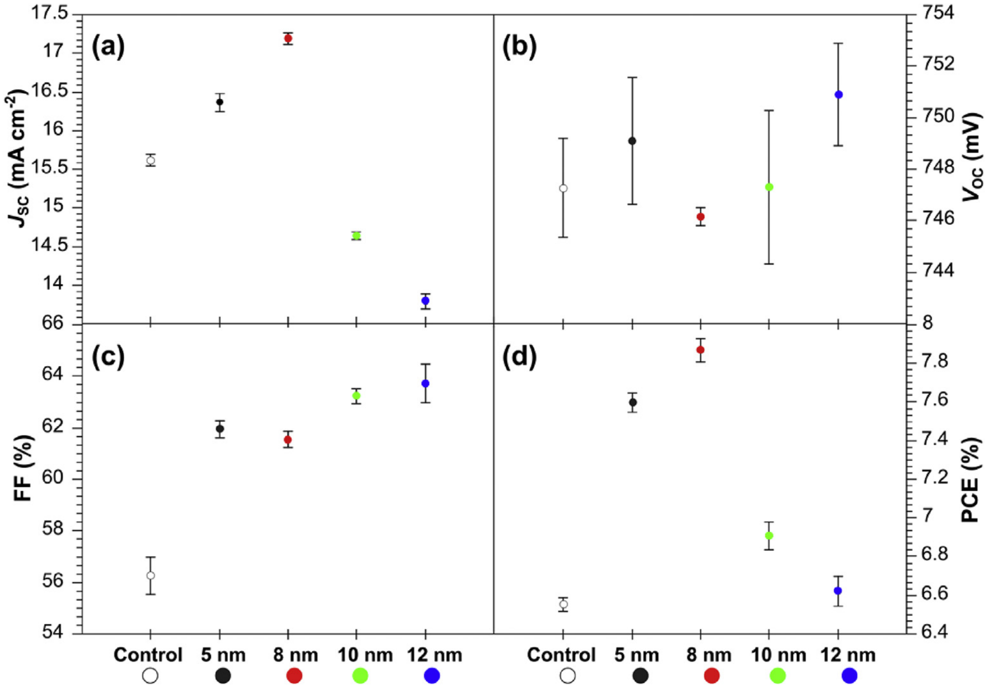

Fig. 5. Average (a) $\boldsymbol{J}_{\mathrm{sc}}$, (b) $\boldsymbol{V}_{\mathrm{oc}}$ (c) FF, and (d) power conversion efficiency (PCE) of the fabricated PECs. The averages were calculated over 5 separate batches of devices and the standard error has been fitted as error bars.

and cause a reduction in $\boldsymbol{V}_{\mathrm{OC}}$ due to the possibility of an alternative current path. Given the $\boldsymbol{V}_{\mathrm{OC}}$ for all devices remained consistent, supports the hypothesis that the increase in PCE can be partly attributed to a decrease in R_S for the TiO_2 NP/AuNP NF devices containing 8 nm AuNPs. Furthermore, dye desorption tests were undertaken and all photoelectrodes were found to have similar dye loading (Table S1). This also agrees with previous work where both the size of AuNPs and the concentration has shown little effect on dye adsorption [19,20].

Furthermore, we performed electrochemical impedance spectroscopy (EIS) to provide a better understanding about the dynamics of electron transport, and reveal the difference in the interfacial characteristics (such as recombination) of the 8 nm AuNPs in the PECs [40]. Fig. 6 shows the Nyquist plots for the TiO_2 NP/TiO_2 NF (control) and TiO_2/AuNP-TiO_2 NF (8 nm AuNPs) measured under dark conditions, ranging from 0.01 Hz to 1000 kHz at an applied bias of -0.700 V. The inset of Fig. 6 represents the equivalent circuit which was adopted to fit the Nyquist spectra. The results reveal two distinguishable semicircles, where the small semicircle is related to the electrochemical reaction at the counter electrode (R_{ct1}) and the large semicircle is related to the TiO_2 photoelectrode/electrolyte interface (R_{ct2}) [40–42]. As depicted in the equivalent circuit, R_S represents the series ohmic resistance which exists in the external circuit, where C_μ is the constant phase element representing the capacitor components in the solar cell. Given the same counter electrode and electrolyte were used in both PECs, there is no apparent difference in R_{ct1} and this can be seen by the almost identical diameters of the first small semicircle for both photoelectrodes (Fig. 6). Interestingly, the electron transport resistance (R_{ct2}) dramatically decreases from 121.8 Ω for the control photoelectrode to 79.0 Ω for the photoelectrode containing the 8 nm AuNPs (Table 2). The decrease in resistance implies improved and faster electron transport and injection rate for the photoelectrodes containing the 8 nm AuNPs. The electron lifetime ($\tau_e = RC_\mu$) [41,43] values were calculated to be 38.0 and 27.1 ms for the control and 8 nm AuNPs PECs, respectively (Table 2). The shorter electron lifetime for the photoelectrode with the 8 nm AuNPs suggests this PEC is slightly more susceptible to recombination between the photoelectrons in the conduction band of the TiO_2 and the redox mediator (I_3^-). This is reflected in the decrease in $\boldsymbol{V}_{\mathrm{OC}}$ which was seen for the 8 nm AuNP PECs compared to the control PECs (Fig. 5b) [41]. However due to the superior reduction in resistance which was evident under both light and dark conditions, and increase in $\boldsymbol{J}_{\mathrm{SC}}$ and FF, the photoelectrodes containing the 8 nm AuNPs had the highest PCE (Fig. 5d).

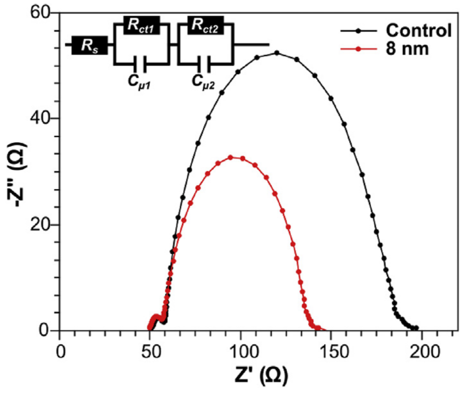

Fig. 6. Nyquist plots for TiO_2 NP/TiO_2 NF (control) and TiO_2/AuNP-TiO_2 NF (8 nm AuNPs) measured under dark conditions and a bias of -0.7 V. The inset shows the equivalent circuit diagram.

Table 2

Electron transport resistance (R_{ct2}), constant phase element ($C_{\mu 2}$), and electron lifetime (τ_e) values for control and 8 nm AuNP PECs.

PEC	R_{ct2} (Ω)	$C_{\mu 2}$ (μF)	τ_e (ms)
Control TiO_2 NFs	121.8	312.1	38.0
8 nm AuNPs	79.0	343.3	27.1

The benefits of adding sub-12 nm AuNPs to the scattering layer of TiO_2 NF PECs has clearly been shown where improvements can be seen across the entire spectral range. In terms of performance, the PECs are to the best of our knowledge one of the highest ever reported for scattering layers based on 100% pure anatase TiO_2 NFs. The current record for NF-based scattering layer PECs was achieved by Chuangchote et al. [44] where they obtained an impressive 8.14% with an active area of 0.25 cm^{-2} and 10.3% for a small active area of 0.05 cm^{-2}. However, their PECs were over 15 μm thick where only 1 μm was that of TiO_2 NFs. This ultrathin scattering layer suggests that some of the performance enhancement was also due to the large amount of high surface area NPs in the PEC. In another report, Naphade et al. [20] fabricated AuNP containing TiO_2 NF DSSCs and achieved a PCE of 7.8%, improving their control NF PECs by 15%, which was similar to the improvement margin demonstrated in this work. However, they did not control the particle size of their AuNPs. In contrast to existing reports, we provide a compressive performance evaluation for precisely size controlled sub-12 nm AuNPs in TiO_2 NF photoelectrodes and determine the upper and lower size limits of incorporating small AuNPs into assembled PECs. Interestingly, the dominating roles of each different sized AuNP was clearly different. For the 5 and 8 nm AuNP based PECs, benefits were seen from increased light harvesting and improved charge transport which resulted in the increased $\boldsymbol{J}_{\mathrm{SC}}$, FF and decrease in the series resistance. On the other hand, the dominating role of the 10 and 12 nm AuNPs was less likely to be due to the light harvesting due to a decrease in the $\boldsymbol{J}_{\mathrm{SC}}$. Despite this, the consistent increase in FF for all AuNP based PECs suggests a reduction in parasitic resistive losses. While the overall PCE was consistently higher for all AuNP based PECs, the highest performing cells were those that contained the 8 nm AuNPs. Therefore, the dominant role of the 8 nm AuNPs is the improvement in the light harvesting from the plasmonic features, decrease in series resistance and increase in electron transport and injection rate.

4. Conclusion

In this paper, we have demonstrated the benefits of adding sub-12 nm AuNPs into the scattering layer of TiO_2 NF photoelectrodes. The composite photoelectrodes were assembled into PECs and the gold loaded photoelectrodes show improvements in the current density and the fill factor which is attributed to increased spectral absorption, decrease in series resistance, and increase in electron transport and injection rate. Compared to the control PECs, devices loaded with 8 nm AuNPs show 20% improvement in average PCE, where the highest performing device obtained an PCE of 8% which is among the highest reported for TiO_2 NF PECs. We show that the precise control over NP size is critical to performance enhancement in TiO_2 NF PECs and we believe that this knowledge will help shape future studies into work incorporating plasmonic NPs into renewable energy applications.

Author contributions

Experiments were designed by T.J.M with guidance from H.Y, I.P, J.G.S, and I.P.P. All PECs were fabricated by T.J.M, F.A, M.B, and Y.L.

Electron microscopy was completed by T.J.M, D.Y, and C.C. The manuscript was written by T.J.M with contributions of all authors. All authors have given approval to the final version of the manuscript.

Acknowledgement

TJM would like to thank the Ramsay Memorial Trust for their financial assistance. T.J.M and I.P.P would like to acknowledge the EPSRC for financial support (EP/M015157/1). T.J.M would also like to thank Dr. Guanjie He for assisting with the EIS measurements. All authors would like to thank Prof. Peter Dobson for the useful discussions.

Appendix A. Supplementary data

Supplementary data related to this article can be found at https://doi.org/10.1016/j.mtener.2018.06.005.

References

[1] A. Fujishima, K. Honda, Electrochemical photolysis of water at a semiconductor electrode, Nature 238 (1972) 37–38, https://doi.org/10.1038/238037a0.

[2] B. O'Regan, M. Gratzel, A low-cost, high-efficiency solar cell based on dye-sensitized colloidal TiO_2 films, Nature 353 (1991) 737–740, https://doi.org/10.1038/353737a0.

[3] J. Tao, T. Luttrell, M. Batzill, A two-dimensional phase of TiO_2 with a reduced bandgap, Nat. Chem. 3 (2011) 296–300, https://doi.org/10.1038/nchem.1006.

[4] M. Gratzel, Photoelectrochemical cells, Nature 414 (2001) 338–344, https://doi.org/10.1038/35104607.

[5] S.U.M. Khan, M. Al-Shahry, W.B. Ingler, Efficient photochemical water splitting by a chemically modified n-TiO_2, Science 297 (2002) 2243–2245, https://doi.org/10.1126/science.1075035.

[6] M.M. Lee, J. Teuscher, T. Miyasaka, T.N. Murakami, H.J. Snaith, Efficient hybrid solar cells based on meso-superstructured organometal halide perovskites, Science 338 (2012) 643–647, https://doi.org/10.1126/science.1228604.

[7] P. Wang, S.M. Zakeeruddin, J.E. Moser, M.K. Nazeeruddin, T. Sekiguchi, M. Grätzel, A stable quasi-solid-state dye-sensitized solar cell with an amphiphilic ruthenium sensitizer and polymer gel electrolyte, Nat. Mater. 2 (2003) 402–407, https://doi.org/10.1038/nmat904.

[8] Y. Cao, Y. Saygili, A. Ummadisingu, J. Teuscher, J. Luo, N. Pellet, F. Giordano, S.M. Zakeeruddin, J.-E. Moser, M. Freitag, A. Hagfeldt, M. Grätzel, 11% efficiency solid-state dye-sensitized solar cells with copper(II/I) hole transport materials, Nat. Commun. 8 (2017) 15390, https://doi.org/10.1038/ncomms15390.

[9] A. Yella, H.-W. Lee, H.N. Tsao, C. Yi, A.K. Chandiran, M.K. Nazeeruddin, E.W.-G. Diau, C.-Y. Yeh, S.M. Zakeeruddin, M. Grätzel, Porphyrin-sensitized solar cells with cobalt (II/III)–based redox electrolyte exceed 12 percent efficiency, Science 334 (2011) 629–634, https://doi.org/10.1126/science.1209688.

[10] U. Bach, D. Lupo, P. Comte, J.E. Moser, F. Weissörtel, J. Salbeck, H. Spreitzer, M. Grätzel, Solid-state dye-sensitized mesoporous TiO_2 solar cells with high photon-to-electron conversion efficiencies, Nature 395 (1998) 583–585, https://doi.org/10.1038/26936.

[11] S. Mathew, A. Yella, P. Gao, R. Humphry-Baker, F.E. Curchod Basile, N. Ashari-Astani, I. Tavernelli, U. Rothlisberger, Md. Khaja Nazeeruddin, M. Grätzel, Dye-sensitized solar cells with 13% efficiency achieved through the molecular engineering of porphyrin sensitizers, Nat. Chem. 6 (2014) 242–247.

[12] K. Kakiage, Y. Aoyama, T. Yano, K. Oya, J. Fujisawa, M. Hanaya, Highly-efficient dye-sensitized solar cells with collaborative sensitization by silyl-anchor and carboxy-anchor dyes, Chem. Commun. 51 (2015) 15894–15897, https://doi.org/10.1039/C5CC06759F.

[13] G.K. Mor, K. Shankar, M. Paulose, O.K. Varghese, C.A. Grimes, Use of highly-ordered TiO_2 nanotube arrays in dye-sensitized solar cells, Nano Lett. 6 (2006) 215–218, https://doi.org/10.1021/nl052099j.

[14] G.K. Mor, K. Shankar, M. Paulose, O.K. Varghese, C.A. Grimes, Enhanced photocleavage of water using titania nanotube arrays, Nano Lett. 5 (2005) 191–195, https://doi.org/10.1021/nl048301k.

[15] X. Feng, K. Shankar, O.K. Varghese, M. Paulose, T.J. Latempa, C.A. Grimes, Vertically aligned single crystal TiO_2 nanowire arrays grown directly on transparent conducting oxide coated glass: synthesis details and applications, Nano Lett. 8 (2008) 3781–3786, https://doi.org/10.1021/nl802096a.

[16] T.J. Macdonald, D.D. Tune, M.R. Dewi, C.T. Gibson, J.G. Shapter, T. Nann, A TiO_2 nanofiber–carbon nanotube-composite photoanode for improved efficiency in dye-sensitized solar cells, ChemSusChem 8 (2015) 3396–3400, https://doi.org/10.1002/cssc.201500945.

[17] M. Batmunkh, T.J. Macdonald, C.J. Shearer, M. Bat-Erdene, Y. Wang, M.J. Biggs, I.P. Parkin, T. Nann, J.G. Shapter, Carbon nanotubes in TiO_2 nanofiber photoelectrodes for high-performance perovskite solar cells, Adv. Sci. 4 (2017), https://doi.org/10.1002/advs.201600504.

[18] S. Muduli, O. Game, V. Dhas, K. Vijayamohanan, K.A. Bogle, N. Valanoor, S.B. Ogale, TiO_2–Au plasmonic nanocomposite for enhanced dye-sensitized solar cell (DSSC) performance, Sol. Energy 86 (2012) 1428–1434, https://doi.org/10.1016/j.solener.2012.02.002.

[19] Q. Wang, T. Butburee, X. Wu, H. Chen, G. Liu, L. Wang, Enhanced performance of dye-sensitized solar cells by doping Au nanoparticles into photoanodes: a size effect study, J. Mater. Chem. A 1 (2013) 13524–13531, https://doi.org/10.1039/C3TA12692G.

[20] R.A. Naphade, M. Tathavadekar, J.P. Jog, S. Agarkar, S. Ogale, Plasmonic light harvesting of dye sensitized solar cells by Au-nanoparticle loaded TiO_2 nanofibers, J. Mater. Chem. A 2 (2013) 975–984, https://doi.org/10.1039/C3TA13246C.

[21] H.-Y. Kim, D.H. Song, H. Yoon, J.S. Suh, Surface plasmon-enhanced dye-sensitized solar cells based on double-layered composite films consisting of TiO_2/Ag and TiO_2/Au nanoparticles, RSC Adv. 5 (2015) 27464–27469, https://doi.org/10.1039/C5RA03677A.

[22] J. Du, J. Qi, D. Wang, Z. Tang, Facile synthesis of Au@TiO_2 core–shell hollow spheres for dye-sensitized solar cells with remarkably improved efficiency, Energy Environ. Sci. 5 (2012) 6914–6918, https://doi.org/10.1039/C2EE21264A.

[23] Y. Li, H. Wang, Q. Feng, G. Zhou, Z.-S. Wang, Gold nanoparticles inlaid TiO_2 photoanodes: a superior candidate for high-efficiency dye-sensitized solar cells, Energy Environ. Sci. 6 (2013) 2156–2165, https://doi.org/10.1039/C3EE23971C.

[24] M.D. Brown, T. Suteewong, R.S.S. Kumar, V. D'Innocenzo, A. Petrozza, M.M. Lee, U. Wiesner, H.J. Snaith, Plasmonic dye-sensitized solar cells using core–shell metal–insulator nanoparticles, Nano Lett. 11 (2011) 438–445, https://doi.org/10.1021/nl1031106.

[25] C. Yogi, K. Kojima, T. Hashishin, N. Wada, Y. Inada, E. Della Gaspera, M. Bersani, A. Martucci, L. Liu, T.-K. Sham, Size effect of Au nanoparticles on TiO_2 crystalline phase of nanocomposite thin films and their photocatalytic properties, J. Phys. Chem. C 115 (2011) 6554–6560, https://doi.org/10.1021/jp110581j.

[26] W.P. Wuelfing, S.M. Gross, D.T. Miles, R.W. Murray, Nanometer gold clusters protected by surface-bound monolayers of thiolated poly(ethylene glycol) polymer electrolyte, J. Am. Chem. Soc. 120 (1998) 12696–12697, https://doi.org/10.1021/ja983183m.

[27] I. Hussain, S. Graham, Z. Wang, B. Tan, D.C. Sherrington, S.P. Rannard, A.I. Cooper, M. Brust, Size-controlled synthesis of near-monodisperse gold nanoparticles in the 1–4 nm range using polymeric stabilizers, J. Am. Chem. Soc. 127 (2005) 16398–16399, https://doi.org/10.1021/ja055321v.

[28] K.B. Male, J. Li, C.C. Bun, S.-C. Ng, J.H.T. Luong, Synthesis and stability of fluorescent gold nanoparticles by sodium borohydride in the presence of mono-6-deoxy-6-pyridinium-β-cyclodextrin chloride, J. Phys. Chem. C 112 (2008) 443–451, https://doi.org/10.1021/jp7099515.

[29] T.J. Macdonald, K. Wu, S.K. Sehmi, S. Noimark, W.J. Peveler, H. du Toit, N.H. Voelcker, E. Allan, A.J. MacRobert, A. Gavriilidis, I.P. Parkin, Thiol-capped gold nanoparticles swell-encapsulated into polyurethane as powerful antibacterial surfaces under dark and light conditions, Sci. Rep. 6 (2016) 39272, https://doi.org/10.1038/srep39272.

[30] J. Piella, N.G. Bastús, V. Puntes, Size-controlled synthesis of sub-10-nanometer citrate-stabilized gold nanoparticles and related optical properties, Chem. Mater. 28 (2016) 1066–1075, https://doi.org/10.1021/acs.chemmater.5b04406.

[31] R. Torres-Mendieta, D. Ventura-Espinosa, S. Sabater, J. Lancis, G. Mínguez-Vega, J.A. Mata, In situ decoration of graphene sheets with gold nanoparticles synthetized by pulsed laser ablation in liquids, Sci. Rep. 6 (2016) 30478, https://doi.org/10.1038/srep30478.

[32] P. Joshi, L. Zhang, D. Davoux, Z. Zhu, D. Galipeau, H. Fong, Q. Qiao, Composite of TiO_2 nanofibers and nanoparticles for dye-sensitized solar cells with significantly improved efficiency, Energy Environ. Sci. 3 (2010) 1507–1510, https://doi.org/10.1039/C0EE00068J.

[33] S. Ito, T.N. Murakami, P. Comte, P. Liska, C. Grätzel, M.K. Nazeeruddin, M. Grätzel, Fabrication of thin film dye sensitized solar cells with solar to electric power conversion efficiency over 10%, 6th Int. Conf. Coat. Glass Plast. ICCG6 Adv. Coat. Large-Area High-Vol. Prod. 516 (2008) 4613–4619, https://doi.org/10.1016/j.tsf.2007.05.090.

[34] M.P. Casaletto, A. Longo, A. Martorana, A. Prestianni, A.M. Venezia, XPS study of supported gold catalysts: the role of Au0 and $Au+\delta$ species as active sites, Surf. Interface Anal. 38 (2006) 215–218, https://doi.org/10.1002/sia.2180.

[35] H. Li, Z. Bian, J. Zhu, Y. Huo, H. Li, Y. Lu, Mesoporous Au/TiO_2 nanocomposites with enhanced photocatalytic activity, J. Am. Chem. Soc. 129 (2007) 4538–4539, https://doi.org/10.1021/ja069113u.

[36] M. Batmunkh, T.J. Macdonald, W.J. Peveler, A.S.R. Bati, C.J. Carmalt, I.P. Parkin, J.G. Shapter, Plasmonic gold nanostars incorporated into high-efficiency perovskite solar cells, ChemSusChem 10 (2017) 3750–3753, https://doi.org/10.1002/cssc.201701056.

[37] P. Zhu, A.S. Nair, S. Yang, S. Peng, S. Ramakrishna, Which is a superior material for scattering layer in dye-sensitized solar cells—electrospun rice grain- or nanofiber-shaped TiO_2? J. Mater. Chem. 21 (2011) 12210–12212, https://doi.org/10.1039/C1JM11939G.

[38] M. Batmunkh, M.J. Biggs, J.G. Shapter, Carbon nanotubes for dye-sensitized solar cells, Small 11 (2015) 2963–2989, https://doi.org/10.1002/smll.201403155.

[39] S. Chang, Q. Li, X. Xiao, K.Y. Wong, T. Chen, Enhancement of low energy sunlight harvesting in dye-sensitized solar cells using plasmonic gold nanorods, Energy Environ. Sci. 5 (2012) 9444–9448, https://doi.org/10.1039/C2EE22657J.

[40] Q. Wang, J.-E. Moser, M. Grätzel, Electrochemical impedance spectroscopic analysis of dye-sensitized solar cells, J. Phys. Chem. B 109 (2005) 14945–14953, https://doi.org/10.1021/jp052768h.

[41] B.-X. Lei, P. Zhang, H.-K. Qiao, X.-F. Zheng, Y.-S. Hu, G.-L. Huang, W. Sun, Z.-F. Sun, X.-X. Zhang, A facile template-free route for synthesis of anatase TiO_2 hollow spheres for dye-sensitized solar cells, Electrochim. Acta 143 (2014) 129–134, https://doi.org/10.1016/j.electacta.2014.07.106.

[42] Y. Wang, Q. Zhang, F. Huang, Z. Li, Y.-Z. Zheng, X. Tao, G. Cao, In situ assembly of well-defined Au nanoparticles in TiO_2 films for plasmon-enhanced quantum dot sensitized solar cells, Nano Energy 44 (2018) 135–143, https://doi.org/10.1016/j.nanoen.2017.11.078.

[43] Z.-Q. Li, W.-C. Chen, F.-L. Guo, L.-E. Mo, L.-H. Hu, S.-Y. Dai, Mesoporous TiO_2 yolk-shell microspheres for dye-sensitized solar cells with a high efficiency exceeding 11%, Sci. Rep. 5 (2015) 14178, https://doi.org/10.1038/srep14178.

[44] S. Chuangchote, T. Sagawa, S. Yoshikawa, Efficient dye-sensitized solar cells using electrospun TiO_2 nanofibers as a light harvesting layer, Appl. Phys. Lett. 93 (2008) 033310–033313.